Atmospheric Environment Vol. 27A, No. 15, pp. 2295–2311, 1993.
Printed in Great Britain.

0004–6981/93 $6.00 + 0.00

A COMPUTATIONAL MODEL FOR THE RISE AND DISPERSION OF WIND-BLOWN, BUOYANCY-DRIVEN PLUMES—I. NEUTRALLY STRATIFIED ATMOSPHERE

XIAOMING ZHANG and AHMED F. GHONIEM†
Department of Mechanical Engineering, Massachusetts Institute of Technology, Cambridge, MA 02139, U.S.A.

(*First received* 20 *November* 1992 *and in final form* 14 *April* 1993)

Abstract—A multi-dimensional computational model for the rise and dispersion of a wind-blown, buoyancy-driven plume in a calm, neutrally stratified atmosphere is presented. Lagrangian numerical techniques, based on the extension of the vortex method to variable density flows, are used to solve the governing equations. The plume rise trajectory and the dispersion of its material in the crosswind plane are predicted. It is found that the computed trajectory agrees well with the two-thirds power law of a buoyancy-dominated plume, modified to include the effect of the initial plume size. The effect of small-scale atmospheric turbulence, modeled in terms of eddy viscosity, on the plume trajectory is found to be negligible. For all values of buoyancy Reynolds number, the plume cross-section exhibits a kidney-shaped pattern, as observed in laboratory and field experiments. This pattern is due to the formation of two counter-rotating vortices which develop as baroclinically generated vorticity rolls up on both sides of the plume cross-section. Results show that the plume rise can be described in terms of three distinct stages: a short acceleration stage, a long double-vortex stage, and a breakup stage. The induced velocity field and engulfment are dominated by the two large vortices. The effect of a flat terrain on the plume trajectory and dispersion is found to be very small. The equivalent radii of plumes with different initial cross-sectional aspect ratios increase at almost the same rate. A large aspect-ratio plume rises slower initially and then catches up with smaller aspect-ratio plumes in the breakup stage. The Boussinesq approximation is found to be valid if the ratio of the density perturbation to the reference density is less than 0.1.

Key word index: Buoyant plumes, vortex simulation, entrainment, vortex method, rise and dispersion.

NOMENCLATURE

A_R	aspect ratio of plume cross-section, $\equiv R_y/R_z$
d	characteristic dimension of plume density profile
f_δ	element core function
g_r	gravitational acceleration
$\tilde{g}(\tilde{x}, t)$	density gradient
h	spatial discretization length in the numerical scheme
H	vertical thickness of plume cross-section
H_T	dimensionless initial plume height, H_T^*/R
l_b	buoyancy length
$\dot{m}_p$	deficient mass flux of the plume, $\equiv -\int \rho_p^*(y^*, z^*) U \, dA$
L	circumference of plume cross-section
L_o	L at $t=0$
M	number of discretization layers across plume–air interface
N	total number of computational elements
p	dimensionless perturbation pressure
Pe_b	buoyancy Peclet number
R	square root of plume cross-sectional area
R_{eq}	equivalent radius of plume cross-section
R^*	radius of plume cross-section
R_y	major (horizontal) scale of elliptical plume cross-section
R_z	minor (vertical) scale of elliptical plume cross-section
Re_b	buoyancy Reynolds number
Re_s	stack exit Reynolds number
t	same as the normalized x coordinate
u, v, w	perturbation velocity components in x, y, z direction, respectively
U	homogeneous wind speed
V	buoyancy velocity, $\equiv \sqrt{\varepsilon R g_r}$
$\tilde{\mathbf{u}}$	velocity vector
W	plume horizontal width
W_o	W at $t=0$
x	horizontal wind direction
$\tilde{x}$	$=(y, z)$
y	horizontal direction normal to the wind direction
z	vertical direction
α_e	turbulent eddy diffusivity
β	entrainment coefficient
Γ_i	circulation of a vortex element
δ	core radius of a vortex/transport element
δA_i	area associated with a computational element
$\delta\rho_p$	density variation across a discretization layer
Δ_c	combination length
Δ_i	insertion length
Δt	time step
$\Delta\chi_i$	distance between neighboring computational elements
ε	plume mass flux ratio
ν_e	turbulent eddy viscosity
ρ_o^*	background air density
ρ_p	dimensionless plume density
ρ_p^*	deficient plume density
ω	streamwise vorticity
$\tilde{\chi}_i$	vortex/transport element trajectory

Superscript

*	dimensional quantities.

†Author to whom correspondence should be addressed.

1. INTRODUCTION

Accurate prediction of buoyant plume rise and dispersion in a turbulent atmosphere is important in many practical applications. Buoyancy represents one of the primary mechanisms governing the motion of plumes generated from sources such as massive fires resulting from the burning of oil spills, uncontrolled oil wells, forest fires, and large-scale explosions (Evans *et al.*, 1986; 1989), and hot exhaust plumes emitted from tall industry stacks (Briggs, 1975; Weil, 1988a), among others. Besides buoyancy, the dispersion of these plumes, which determines their impact on the local, and possibly distant environment, is governed by the meteorological conditions, atmospheric turbulence, atmospheric stratification, ground terrain, etc. In this paper, we apply Lagrangian numerical techniques utilizing vortex and transport element methods to solve equations governing a plume rising in a cross-wind in the case of a neutrally stratified atmosphere. Cases involving inversion layers, continuous atmospheric stratification, large-scale atmospheric turbulence, particulate matter and chemical reactions will be studied later.

Most plume studies, including analytical and numerical models, and laboratory and field experiments, can be divided into two categories. The first is concerned with the plume trajectory. Scaling laws for the trajectory of buoyancy-dominated plumes have been proposed (Briggs, 1975, Netterville, 1990). In deriving these laws: (1) the integral equations of volume, mass, and momentum conservation are applied; (2) an entrainment assumption, stating that ambient air influx velocity into the plume is proportional to the velocity difference between the plume and the wind, is used; and (3) a self-similarity profile, Gaussian or top-hat distribution of momentum, buoyancy and pollutant concentration in the plume cross-sections, is introduced (see Appendix for detail and extension). The second category is concerned with the study of plume material dispersion (Venkatram, 1988; Weil, 1988b), including the effects of the atmospheric boundary layer and atmospheric stratification (Deardorff, 1970; Nieuwstadt, 1992a, b). Fundamentally, plume rise and dispersion are strongly interrelated (Nieuwstadt, 1992a, b), and fast dispersion often results from strong entrainment. Buoyancy not only contributes to plume rise, but also to dispersion. In general, for a buoyant material, one cannot independently calculate the plume rise and the dispersion.

Plume rise and dispersion studies have been used to: (1) improve our understanding of plume dynamics and the effect of atmospheric and emission conditions on the spread of pollutants; (2) provide data for atmospheric contamination in specific cases; and (3) contribute, using accurate experimental data, to the development of working models. However, these models, although revealing, can hardly be extended to more complicated problems, such as plume interaction with inversion layers, the effect of complex ground terrains, or cases when physical or chemical transformations of the plume material are important. Empirical constants built into these models, like the entrainment rate, are not universal (Gebhart *et al.*, 1984), and a wide range is reported for their values (Fay *et al.*, 1970; Hewett *et al.*, 1971).

Large-eddy simulation of plumes in the convective boundary layer have recently been performed. In a large-eddy simulation, one computes the large-scale turbulent motion explicitly on a computationally manageable grid, while the effect of the small scales is represented with the aid of a "subgrid model". Since the incorporation of buoyancy effects into turbulence models has not been well established yet, as pointed out by Golay (1982), the description of the strong concentration gradient near the plume interface is not expected to be accurate. One major effect of plume buoyancy is to increase dispersion by self-generated turbulence. This effect is almost completely neglected in large eddy modeling. Furthermore, grid-based numerical methods, including finite-difference or finite-element approaches, involve numerical diffusion which reduces the effective Reynolds number of the simulations. Using a large-eddy model, Nieuwstadt (1992a, b) found that, for a modestly buoyant plume, the calculated concentration distributions were comparable with the experimental results. However, the calculated plume rise did not follow the well-established two-thirds law, and the often observed formation of the two counter-rotating vortices in the plume cross-section was also not accurately resolved. Nieuwstadt suggested that these simulation results be considered with caution.

Numerical simulations of plume rise and dispersion without invoking entrainment hypotheses are still needed. A detailed understanding and accurate prediction of the buoyancy-driven turbulent entrainment process are undoubtedly useful in practice. This paper is an attempt in this direction, considering only buoyant plume motion in a neutral atmosphere with small-scale atmospheric turbulence. The computational model is validated by comparing its results to available experimental data. Increasing the level of complexity, i.e. considering more interactions between the plume and its surroundings, will be dealt with in future publications.

This paper is organized as follows. The assumptions and formulation are discussed in Section 2. Section 3 is a brief summary of the vortex method and transport element method. Section 4 focuses on the study of the effects of buoyancy and small-scale atmospheric turbulence on the plume trajectory. Comparison with the two-thirds power law is presented. In Section 5, plume entrainment and dispersion characteristics are discussed. Field and laboratory observations are used in the comparison with the numerical results. The vorticity generation mechanism, traced back to buoyancy, is then delineated. The effects of the initial plume shape and height are investigated. In Section 6, the validity of the Boussinesq approxima-

tion in the buoyant plume study is investigated. Section 7 is a short conclusion.

2. FORMULATION

2.1. *Scales*

Before presenting the governing equations, we define several important scales in the buoyant plume problem. Let R denote the length scale of the plume cross-section, taken here as the square root of the initial plume cross-sectional area. The atmosphere is assumed to be neutrally stratified with constant density ρ_o^* and uniform horizontal wind velocity U. The initial plume density distribution is $\rho_o^*+\rho_p^*$ where $\rho_p^*(y^*, z^*)$ is the deficient plume density, which is negative for a high temperature, low density rising plume. The deficient plume mass flux is

$$\dot{m}_p = -\int \rho_p^* U \, dA > 0. \tag{1}$$

A suitable buoyancy velocity scale is

$$V = \sqrt{\varepsilon R g_r} \tag{2}$$

where

$$\varepsilon = \frac{\dot{m}_p}{\rho_o^* U R^2} \ll 1 \tag{3}$$

is the mass flux ratio, i.e. the ratio between the deficient plume mass flux and the air mass flux within the plume cross-section, and g_r is the gravitational acceleration. For a typical plume, $|\rho_p^*/\rho_o^*| \approx O(10^{-1})$, so that $\varepsilon \approx O(10^{-1})$. Thus, for $R = O(10\ \text{m})$, a characteristic buoyancy velocity is $V = O(3\ \text{m s}^{-1})$. This velocity scale is smaller than the usual ambient wind velocity $U \approx O(5\text{–}10\ \text{m s}^{-1})$.

A buoyant Reynolds number can be defined as

$$Re_b = \frac{VR}{\nu_e} \tag{4}$$

where ν_e is the small-scale turbulent eddy viscosity.†

2.2. *Governing equations*

The goal of our study is to predict, using numerical simulations, the downwind trajectory and dispersion of the plume material, or the distribution of ρ_p^*. The problem is illustrated schematically in Fig. 1. The following assumptions are used to simplify the formulation without removing important physical processes

(1) the plume motion is steady;
(2) the initial plume cross-section is elliptical;

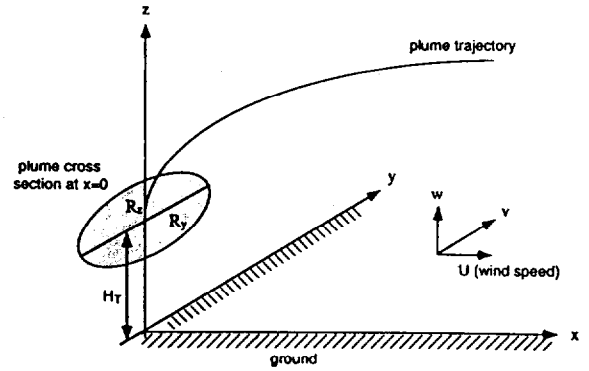

Fig. 1. Schematic diagram showing the plume trajectory and coordinate system.

(3) the plume is advected with a uniform wind velocity U along x^*-axis;‡
(4) the trajectory length scale is much larger than the size of the plume cross-section. This assumption eliminates the small-scale irregularities of the plume in the wind direction (Weil, 1988a);
(5) wind stratification and density stratification effects are neglected;
(6) the effect of large-scale atmospheric turbulence is neglected and the plume buoyancy dominates the motion;§
(7) the eddy viscosity ν_e and eddy diffusivity α_e, modeling the small-scale turbulence, are assumed to have equal values; and
(8) the fluid is incompressible, as justified by Luti and Brzustowski (1977) and Briggs (1984).

These assumptions are used to simplify the physical model; an essential first step in the development and validation of the numerical scheme. In future work, these assumptions will be relaxed and the computational model expanded to include, e.g. atmospheric density stratification and near-ground turbulence (Zhang and Ghoniem, 1993).

Denote the perturbation velocity, or the velocity induced due to buoyancy, by (u^*, v^*, w^*), the components in the horizontal wind direction, x^*, horizontal

†In this paper, we loosely differentiate between large-scale and small-scale turbulence using the plume radius as a characteristic length scale. We only account for the effect of turbulent eddies whose size is much smaller than the plume radius. The effect of these eddies is to enhance turbulent diffusion. The effect of larger scales will be studied in future work.

‡Note that the transfer of the horizontal momentum is essentially complete within a few, about 5, exit diameters from the emission source and the plume thereafter travels at a horizontal speed indistinguishable from the wind speed (Csanady, 1973).

§The effect of plume buoyancy relative to atmospheric turbulence can be assessed by a Richardson number

$$R_i \equiv \frac{g_r(\Delta\rho^*)R}{\rho_o^* w'^2}$$

where $\Delta\rho^*$ is the density difference across the plume surface, and w' is a characteristic atmospheric velocity in the vertical direction. For values of $R_i > 1$, corresponding to large plumes such as fire plumes, buoyancy is expected to be the dominant effect. For example, consider a fire plume with $R \sim 10$ m and $\Delta\rho^*/\rho_o^* \sim O(10^{-1})$ in a $w' \sim O(1\ \text{m s}^{-1})$ atmospheric turbulence, $R_i \sim O(10)$.

crosswind direction, y^*, and the vertical z^*-direction, respectively. The governing equations are the three-dimensional, steady Navier–Stokes equations with $u^*/U \ll 1$. We define the dimensionless variables as follows

$$(y, z)=(y^*, z^*)/R$$

$$(v, w)=(v^*, w^*)/V$$

$$t=x=\frac{x^*/U}{R/V}=\frac{x^*}{U}\sqrt{\frac{\varepsilon g_r}{R}}$$

$$\rho_p=\frac{\rho_p^*}{\varepsilon\rho_o^*} \tag{5}$$

$$p=\frac{p^*}{\rho_o^* V^2}$$

$$\rho=\frac{\rho_o^*+\rho_p^*}{\varepsilon\rho_o^*}=\frac{1}{\varepsilon}(1+\varepsilon\rho_p).$$

The length scale in the x^*-direction is $U\sqrt{R/\varepsilon g_r}$, and for a reason which will become clear soon, the dimensionless x has been written as t. The normalized governing equations are

$$\frac{\partial v}{\partial t}+v\frac{\partial v}{\partial y}+w\frac{\partial v}{\partial z}+\frac{1}{1+\varepsilon\rho_p}\frac{\partial p}{\partial y}=\frac{1}{Re_b}\nabla^2 v \tag{6}$$

$$\frac{\partial w}{\partial t}+v\frac{\partial w}{\partial y}+w\frac{\partial w}{\partial z}+\frac{1}{1+\varepsilon\rho_p}\frac{\partial p}{\partial z}+\frac{\rho_p}{1+\varepsilon\rho_p}=\frac{1}{Re_b}\nabla^2 w \tag{7}$$

$$\frac{\partial v}{\partial y}+\frac{\partial w}{\partial z}=0 \tag{8}$$

$$\frac{\partial \rho_p}{\partial t}+v\frac{\partial \rho_p}{\partial y}+w\frac{\partial \rho_p}{\partial z}=\frac{1}{Pe_b}\nabla^2\rho_p \tag{9}$$

where $Pe_b=VR/\alpha_e$ is the turbulent buoyancy Peclet number ($Pe_b=Re_b$ in this work) and $\nabla^2=\partial^2/\partial y^2+\partial^2/\partial z^2$. The perturbation velocity in equations (6)–(9) stands for the instantaneous velocity averaged over the smallest numerically resolvable scale. The effects of eddies with even smaller scales are introduced in the form of a turbulent eddy viscosity and eddy diffusivity. As will be shown in the next section, the numerical resolution is defined by the size of the vortex-element core. Within the element core, variables are distributed according to an assigned "core" function which, to simulate diffusion, evolves in time in a way that depends on Re_b. The solution constructed here, thus, can be considered as a large-eddy simulation of the plume motion in which the large scales are captured by solving the governing equations while the small scales are modeled phenomenologically.

Replacing x by t makes equations (6)–(9), governing the steady plume dispersion, the same as the Navier–Stokes equations of an unsteady, two-dimensional, incompressible flow in a gravitational field. The corresponding vorticity transport equation is obtained by cross differentiating these equations to eliminate p

$$\frac{\partial\omega}{\partial t}+v\frac{\partial\omega}{\partial y}+w\frac{\partial\omega}{\partial z}+\frac{1}{(1+\varepsilon\rho_p)^2}\frac{\partial\rho_p}{\partial y}-\frac{\varepsilon}{(1+\varepsilon\rho_p)^2}\times\left[\frac{\partial\rho_p}{\partial y}\frac{\partial p}{\partial z}-\frac{\partial\rho_p}{\partial z}\frac{\partial p}{\partial y}\right]=\frac{1}{Re_b}\nabla^2\omega \tag{10}$$

where $\omega=\partial w/\partial y-\partial v/\partial z$ is the dimensionless vorticity. Note that the Boussinesq approximation, which corresponds to setting $\varepsilon=0$, has not been implemented. In Section 6, we discuss the range of ε in which this approximation is valid and the characteristics of the non-Boussinesq solution.

The final governing equations are (8), (9) and (10). The required pressure gradient in equation (10) can be obtained from the momentum equations (6) and (7)

$$\frac{\partial p}{\partial y}=-(1+\varepsilon\rho_p)\frac{Dv}{Dt}+\frac{(1+\varepsilon\rho_p)}{Re_b}\nabla^2 v$$

$$\frac{\partial p}{\partial z}=-\rho_p-(1+\varepsilon\rho_p)\frac{Dw}{Dt}+\frac{(1+\varepsilon\rho_p)}{Re_b}\nabla^2 w \tag{11}$$

where

$$\frac{D}{Dt}\equiv\frac{\partial}{\partial t}+v\frac{\partial}{\partial y}+w\frac{\partial}{\partial z}.$$

The initial conditions are defined in terms of the initial plume cross-section, which is taken here to be an ellipse symmetric about $y=0$. The ellipse has a major axis R_y and a minor axis R_z, and its center is at a distance $H_T=H_T^*/R$ above the ground. This choice is motivated by the observation that as the plume rises, after the initial momentum-dominated stage, its originally circular cross-section is distorted into an ellipse. If we assume that the initial plume has uniform density, then from equations (1), (3) and (5), $\rho_p=-\int dA/R^2=-1$. Using the above normalization, the parameters governing the problems are reduced to the aspect ratio, $A_R=R_y/R_z$, height, H_T, buoyancy Reynolds numer, Re_b, and the mass flux ratio, ε. In the Boussinesq approximation, ε is absent from the governing equations so the number of dimensionless parameters is reduced to three.

3. NUMERICAL SCHEME

In the grid-free, Lagrangian, vortex method, the essential ingredient of the flowfield, the vorticity, is captured by the action of discrete, finite size, overlapping vortex elements whose size, strength and location are determined by approximately satisfying the governing equations. The vorticity field, ω, is discretized among vortex elements, with finite cores, which move along fluid particle trajectories, $\tilde{\chi}_i(t)$ such that

$$\omega(\tilde{x}, t)=\sum_{i=1}^{N}\Gamma_i(t) f_\delta(\tilde{x}-\tilde{\chi}_i(t)) \tag{12}$$

where $\Gamma_i=\omega_i\delta A_i$, ω_i and δA_i are the circulation, vorticity and the area associated with the ith element,

respectively, N is the total number of vortex elements (Ghoniem *et al.*, 1988b), $\vec{x}=(y, z)$ and t is time. The vorticity of an element is distributed according to a radially symmetric core function, f_δ, with a characteristic radius, δ, such that most of the vorticity is concentrated within $r<\delta$, where $r^2=(y-y_i)^2+(z-z_i)^2$. Initially, the vortex elements are distributed over the plume–air interface such that the distance between neighboring elements is h in the two principal directions. A Gaussian core, $f_\delta(r/\delta)=\exp(-r^2/\delta^2)/(\pi\delta^2)$, leads to a second-order accurate scheme (Beale and Majda, 1982a, b).

The equations describing the vortex algorithm are:

$$\frac{d\vec{\chi}_i}{dt}=\vec{u}(\vec{\chi}_i(t), t) \tag{13}$$

with initial positions $\vec{\chi}_i(0)=\vec{X}_i$, where the advection velocity is obtained from the desingularized Biot–Savart law

$$\vec{u}(\vec{x}, t)=-\sum_{i=1}^{N}\Gamma_i\frac{(z-z_i,-y+y_i)}{r^2}\kappa\left(\frac{r}{\delta}\right) \tag{14}$$

while $\kappa(r)=[1-\exp(-r^2)]2\pi$.

The change in the circulation of each element, which depends on the local density gradient, is calculated from the vorticity equation as will be shown shortly. As time progresses, the distance between neighboring elements increases in the direction of maximum strain rate. This leads to a deterioration of the discretization accuracy which requires that $\delta>\Delta\chi$, $\Delta\chi$ being the distance between the centers of the elements. Thus, an algorithm is used such that when $\Delta\chi>\Delta_i$, where Δ_i is the maximum allowable distance between neighboring elements, an element is divided into two elements. The circulation of each of the two new elements is one-half of the circulation of the original element, while the vorticity is the same. The distance between neighboring elements may also decrease due to negative strains. This should be avoided since while it does not improve the spatial accuracy it leads to an unnecessary increase in the computational cost. Thus, when two nearby elements are too close so that $\Delta\chi<\Delta_c$, where Δ_c is the minimum allowable distance between neighboring elements, the two elements are combined into one whose circulation equals the sum of the original two elements (Ghoniem *et al.*, 1988a, b).

The time marching algorithm for the integration of equation (13) uses Heun's second-order predictor–corrector scheme (Dahlquist *et al.*, 1974):

$$\begin{aligned}\vec{\chi}^*&=\vec{\chi}^t+\vec{u}(\vec{\chi}^t)\Delta t\\ \vec{\chi}^{t+\Delta t}&=\vec{\chi}^t+0.5(\vec{u}(\vec{\chi}^t)+\vec{u}(\vec{\chi}^*))\Delta t\end{aligned} \tag{15}$$

where Δt is the time step.

In updating the circulation of a vortex element, the density gradient is required. For this purpose, we use the transport element method (Krishnan and Ghoniem, 1992). This method is a natural extension of the Lagrangian vortex method in which scalar gradients, instead of scalar values, are used in the transport process. The adaptive grid-free form of the calculation allows one to simulate flow in an infinite domain while concentrating all the effort around zones of strong gradients.

To perform the computations, the gradient of the scalar, taken here as the density ρ_p, is discretized among a number of discrete elements such that

$$\vec{g}(\vec{x}, t)=\sum_{i=1}^{N}\vec{g}_i(t)\,\delta A_i f_\delta(\vec{x}-\vec{\chi}_i(t)) \tag{16}$$

where $\vec{g}=\nabla\rho_p$. Like vortex elements, transport elements are distributed where $|\vec{g}|>0$ and are convected with the local velocity field. Density gradients are not conserved along a particle trajectory, but are modified according to the local straining and tilting of the material elements. The values of the density are obtained by direct summation over the field of transport elements

$$\rho_p(\vec{x}, t)=\sum_{i=1}^{N}\vec{g}_i(t)\frac{(y-y_i, z-z_i)}{r^2}\kappa\left(\frac{r}{\delta}\right) \tag{17}$$

where

$$\vec{g}_i(t)=\frac{\delta\rho_{pi}|\delta\vec{\chi}_i(t)|}{\delta A_i}\vec{n}_i(t). \tag{18}$$

In equation (18), $\delta\rho_{pi}$ is the density variation across a layer, $\vec{n}_i(t)$ is the unit vector in the direction of the density gradient, $\delta\vec{\chi}_i$ is the length of an element along a layer. With new elements introduced where excessive stretching is encountered, the scheme maintains high resolution well into the late stages of flow development after high concentration of vorticity and sharp density gradients have evolved. (For more detail, see Krishnan and Ghoniem, 1992; Knio and Ghoniem 1991, 1992.)

In order to simulate the effect of diffusion in both of the vorticity and density transport equations, operator splitting is used. For variable vorticity, the diffusion equation is written for each element

$$\frac{\partial\omega_i}{\partial t}=\frac{1}{Re_b}\nabla^2\omega_i. \tag{19}$$

Therefore, for a vortex element with a Gaussian distribution of vorticity, we have

$$\frac{d\delta^2}{dt}=\frac{4}{Re_b} \tag{20}$$

whose solution is

$$\delta^2=\delta_o^2+\frac{4t}{Re_b} \tag{21}$$

where δ_o is the initial core radius of the element. Thus, the effect of diffusion can be simulated by expanding the core radius as a function of time according to equation (21). This is done without changing the shape of the core function or the values of Γ_i and $\vec{g}_i$. If $Pe_b\neq Re_b(v_c\neq\alpha_c)$, different core sizes should be used for the vortex element and the transport element.

In the present study, the boundary conditions at the ground $z=0$ are: the normal velocity and the material flux vanish. These are satisfied by including the effect of the images of the vortex and transport elements at $z<0$. To avoid repeated calculations, we also impose images of vortex elements at $y<0$, assuming that the plume cross-section maintains its initial symmetry across the original symmetry line, $y=0$. Since the plume height is mostly well above the viscous boundary layer, the effect of this thin layer is neglected.

We discretize the zone of finite density gradient within the plume cross-section into M layers. The density along each layer is constant. The number of layers used depends on the distance across which the density changes from the value inside the plume to the value in the atmosphere. If this distance is very small, one layer is sufficient, otherwise more layers are necessary to maintain acceptable numerical resolution. The number of elements used to describe each layer increases as generated vorticity intensifies and the plume shape becomes increasingly convoluted.

Before we started the simulation of the cases of interest, we conducted a numerical study for the purpose of: (1) showing that the numerical solution converges as the resolution is refined; and (2) determining the optimal values of the numerical parameters which can be used to minimize the CPU time while maintaining the necessary accuracy (Ghoniem *et al.*, 1991)†. The numerical parameters, which control the accuracy of the numerical method (see Fig. 2), are found to be optimal for the following values: the spatial resolution $h=0.025$, the vortex element core radius, $\delta=1.3\,h$, the number of layers, $M=2$, the time step, $\Delta t=0.025$, the insertion length, $\Delta_i=\delta$ and the combination length, $\Delta_c=\delta$. In the calculation, the Boussinesq approximation is used, except in Section 6. The density changes from that of plume to the air density linearly across the plume–air boundary. The length scale in the direction of the density gradient between the plume and the surrounding, normalized with respect to R, is $d=0.1$.

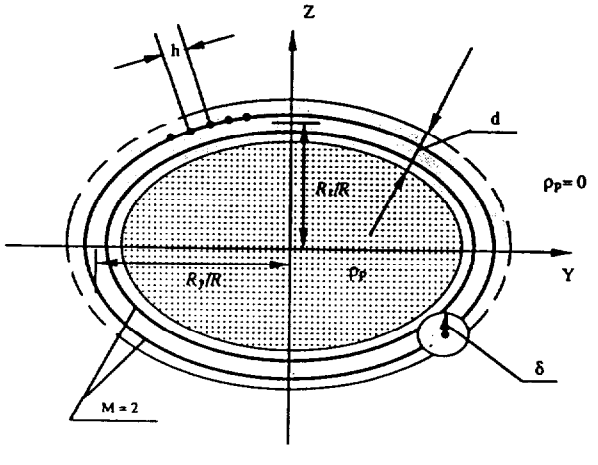

Fig. 2. Schematic diagram showing the physical parameters used to define the geometry of the plume cross-section and the numerical parameters used to discretize the vorticity and density gradient fields. The two thin ellipses show two constant density lines representing the transitions between the plume core and the surrounding air. The two thick ellipses show the layers where the computational elements locate (dark dots) initially.

†Convergence and accuracy were defined in terms of global or integral parameters such as the plume trajectory and overall dimensions of its cross-section.

4. THE TRAJECTORY OF A BUOYANT PLUME

4.1. *Review of studies on plume trajectory*

The scaling length of buoyant motion in a crosswind, called the buoyancy length (Briggs, 1975), can be defined in terms of the notation adopted in this paper, as

$$l_b=\frac{1}{\pi}\left|\frac{\rho_p^*}{\rho_o^*}\right|\frac{g_r R^2}{U^2}. \tag{22}$$

For strongly buoyant plumes, the two-thirds law

$$\frac{\bar{z}^*}{l_b}=\left(\frac{3}{2\beta^2}\right)^{1/3}\left(\frac{x^*}{l_b}\right)^{2/3} \tag{23}$$

has been shown to approximate the trajectory, where $\bar{z}^*$ is the plume center rise and x^* is the downwind distance from the source (Weil, 1988a; Briggs, 1975). The value of entrainment rate, β, is obtained by fitting the scaling law (23), to experimental data. It is found that β also depends on w_o/U, where w_o is the initial vertical exit velocity of the plume.

Laboratory and field experiments have been performed to find the value of β. The plume trajectory is determined by the height of the center of the cross-section, defined as the average, at each crosswind section, of the highest and lowest points on the plume boundary, both identified from photographs (Fay *et al.*, 1970). It should be noted that this height is not necessarily the centroid height of the crosswind plume section if the latter is not vertically symmetric. Here we distinguish between these two as center height (local average) and centroid (mass mean) height. Laboratory experiments (Hewett *et al.*, 1971) showed that the dependence of the plume trajectory on the stack Reynolds number, $Re_s=2w_o r_o/\nu$, where r_o is the radius of the stack, is small, provided the plume is turbulent at the stack exit. The local atmospheric turbulence effect is found to be small and so it is neglected in the scaling law.

4.2. *Extension of the two-thirds law*

The conventional two-thirds power law, equation (23), applies during the stage when buoyancy dominates the plume motion and the initial plume size is negligible (point source). In the case of a massive fire plume, the initial vertical momentum is negligible but the initial plume size is not. To account for the latter, we extended the two-thirds power law (see Appendix).

The resulting expression for a strongly buoyant plume, written in a dimensionless form, is

$$(\sqrt{\pi}\beta z+1)^3-1=\frac{3\sqrt{\pi}\beta}{2}x^2. \tag{24}$$

4.3. *Simulation results*

Three simulations, with same initial circular cross-section, $R_y=R_z=0.5642\,R$, were performed for different buoyancy Reynolds numbers. In all cases, the initial plume height is $H_T=30$ and hence the ground effect is negligible. Figure 3 shows a comparison between the center trajectories of the three plumes and the extended two-thirds law, equation (24), for $\beta=0.7$. Since more computational elements are required in calculating the higher Reynolds number flow, those cases were terminated earlier. It is seen that the rising plume trajectory is generally independent of the buoyancy Reynolds number (at least when buoyancy dominates). Thus, the effects of molecular diffusion and small-scale turbulence on the trajectory are negligible. This is consistent with most experimental observations (Hewett *et al.*, 1971). The computed trajectories are not smooth because of the fluctuations associated with the buoyancy generated turbulence. The trajectory agrees well with the extended two-thirds law when $\beta=0.7$. The conventional (point source) two-thirds law, equation (23), with the suggested (Briggs, 1984) entrainment ratio of $\beta=0.6$ is also shown.

The plume starts with $w_o=0$. As it is accelerated, the generated vorticity at plume surface changes the shape of the cross-section and modifies the vertical velocity. Detailed study of the plume cross-sectional shape and entrainment characteristics are delayed to the next section. Here, it suffices to mention the following. Part of the initial potential energy of the plume is transformed into kinetic energy which is distributed between the plume and the surrounding atmosphere. The rotational velocity induced by the plume sets up an entrainment field towards the plume center. The plume rising velocity is much smaller than that of a solid body of same density because the plume potential energy does not completely transform into plume kinetic energy as in the case of a solid body.

The effect of the initial plume height is determined by simulating the rise of two plumes whose initial cross-sections have the same circular shape but with $H_T=1$ and 30. The first case is close to the situation of a ground fire, while the second is designed so that the ground does not affect the plume motion. Figure 4 shows that the two trajectories are very close. The plume trajectory is thus almost independent of the initial height, with the plume released closer to the ground staying slightly lower than the one released higher. We emphasize that this conclusion applies only when the atmosphere is calm, i.e. when atmospheric turbulence near the ground is weaker than the buoyancy effects. In future work, we plan to extend our modeling to include the effects of wind shear and atmospheric turbulence.

When the initial shape of the plume cross-section is that of an ellipse, the aspect ratio may have some effect on its trajectory. Figure 5 exhibits the three trajectories, $A_R=1, 2, 3$. We can see that the larger A_R plume rises slowly at the beginning, then at around $x=15$, surpasses the lower A_R plume.

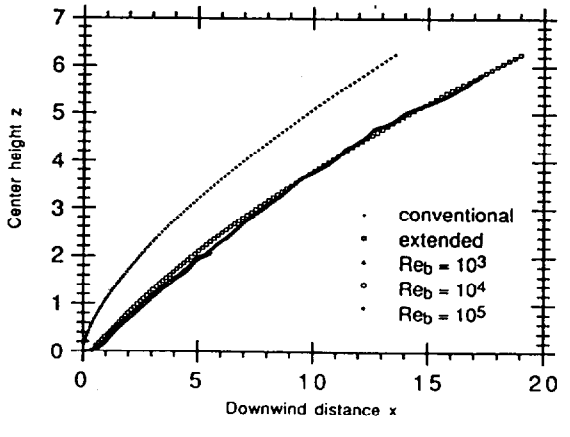

Fig. 3. Trajectories of plume center for $A_R=1$, $H_T=30$, and different buoyant Reynolds numbers, obtained from the numerical simulations, the conventional two-thirds power law and the extended two-thirds power law.

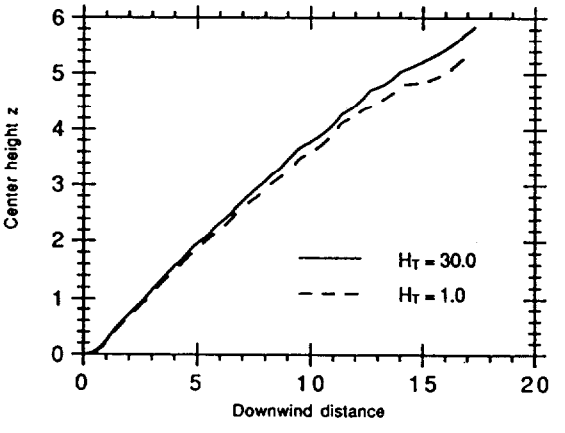

Fig. 4. Trajectories of plume center for $A_R=1$, $Re_b=10^3$, with and without ground effect.

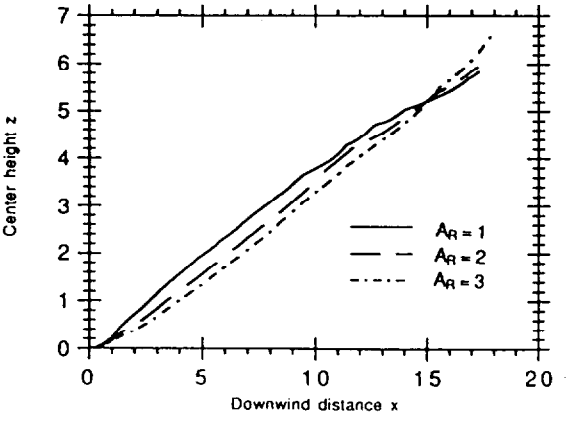

Fig. 5. Trajectory of plume center for $H_T=30$, $Re_b=10^3$, for different aspect ratios.

As will be shown in the next section, the plume cross-section, over most of its history, resembles an inverted kidney-shape. Thus, its centroid (mean mass center) is not the same as its center. To confirm this conclusion using our numerical simulation, we plot the centroid and the center trajectories in Fig. 6. These plots show that the calculation of plume rise in terms of the center height may underestimate the maximum concentration near the ground. Although the trajectory of the centroid is of more interest, it is difficult to measure in practice.

5. DISPERSION

5.1. *Review of plume dispersion studies*

Plume dispersion is strongly related to its trajectory. In the literature, however, most studies calculate the pollutant distribution as if a non-buoyant plume was released from the maximum height it reaches. The most widely used model is that of Pasquill–Gifford–Turner which adopts the Gaussian plume equation and assumes that the lateral and vertical dispersion parameters are given by the Pasquill curves (Turner, 1970; Gifford, 1975; Seinfeld, 1986). As mentioned before, rise and dispersion, being manifestations of the same dynamics, are interrelated, (Nieuwstadt, 1992a).

It is often observed that the distribution of the plume material does not fit a Gaussian profile. Rather, the plume cross-section is kidney-shaped (Briggs, 1975; Abdelwahed and Chu, 1978, etc.). In their laboratory experiment, Hewett *et al.* (1975) showed that the cross-section was not completely circular, but kidney-shaped, and Briggs (1975) proposed a distribution of various quantities within this kidney-shaped cross-section. Moreover, under certain conditions, the plume could split into two separate plumes. Fanaki (1975) observed that bifurcated plumes, forming two lumps with an in-between region where the pollutant concentration is relatively low, traveled downwind forming two counter-rotating line vortices. It was also suggested that bifurcation may reduce the rise of the plume and lead to a horizontal scale larger than the vertical scale. An instrumented aircraft was used to measure the concentration profiles within a bifurcated plume (Janseen *et al.*, 1990). These measurements confirmed the persistent nature of the two line vortices even after evidence of the plume was no longer present. Janseen *et al.* (1990) concluded that the Gaussian concentration profiles could not be used to represent the inhomogeneities in the concentration field.

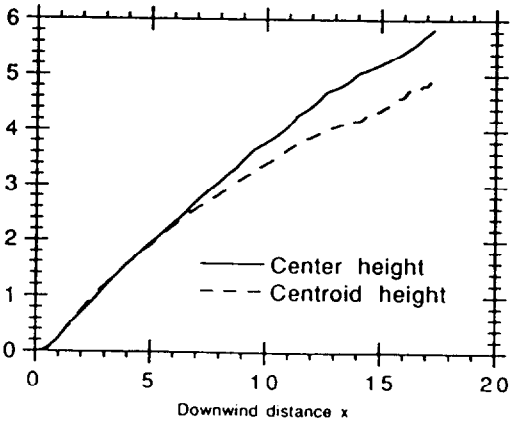

Fig. 6. Trajectories of plume center and centroid for $A_R = 1$, $H_T = 30$ and $Re_b = 10^3$.

The double-vortex structure has also been observed in experimental (Tsang, 1971), analytical (Csanady, 1965) and numerical (Lilly, 1964; Meng and Thomson, 1978) studies on rising two-dimensional thermals. The significance of these observations in the study of plumes stems from the fact that the equations governing the dynamics of bent-over plumes, equations (6)–(9), are identical to those governing rising thermals. Thus, it is expected that the governing dynamics of both flow phenomena to be similar.

Investigations into the mechanism of the formation of this kidney-shaped cross-section and bifurcation have followed two lines. The first suggests that the interaction between the crosswind and a non-buoyant jet may be the cause of this distortion. McMahon *et al.* (1971) described the process of vortex shedding that occurred when a crossflow felt the presence of a non-buoyant jet as essentially a solid object. The effect of this vortex shedding, associated with the pressure drag on the plume, was to distort the shape of the plume and induce streamwise (with respect to the plume stream) vorticity into the flow. Crabb *et al.* (1981) and Sherif and Pletcher (1989) performed several experiments and showed that a wake forms behind a non-buoyant jet due to the presence of crosswind. Near the exit of a stack, moderate wind develops shear stresses on the opposite sides of the plume thereby inducing vorticity with opposite signs at these points. The effectiveness of this mechanism depends on the initial momentum of the jet. On the other hand, Hewett *et al.* (1971), using 547 measurements within the plume cross-section, showed that a kidney-shaped section formed even when the initial momentum was negligibly small. This suggest that the bifurcation phenomenon be independent of the plume initial momentum.

Another mechanism proposed to explain this distortion is buoyancy. The bent plume is more buoyant at its core where the density is the lowest and thereby rises faster at center. Turner (1959) assumed that the flow within the plume was similar to that generated by a vortex pair with fixed circulation and showed that the bifurcation of the plume results from the lateral separation of the vortex pair. However, how the plume acquired this circulation was not explained in detail. Scorer (1958) concurred that the internal circulation, induced by buoyancy, caused the plume to bifurcate while Moore (1966) indicated that for a non-turbulent flow, the plume remained continuous and bifurcation might persist for thousands of meters

downwind. Khandekar and Murty (1975) claimed that the existence of an atmospheric elevated inversion layer was crucial to the separation of these vortices.

Having realized the kidney-shaped structure of the rising plume. Schwartz and Tulin (1972) developed a model based on the dynamics of a vortex pair. The trajectory evaluated using this model also followed the two-thirds power law. Recently, the role of the concentration fluctuations in plume dispersion has come under investigation (Sykes, 1988). Since our numerical simulation can capture some of the small-scale fluctuations, it can provide some insights into the mechanism of the distortion of plume cross-section.

5.2. *Plume cross-section and vorticity generation*

Figure 7 depicts the evolution of the cross-section of a plume with $Re_b = 10^3$, while the table shows the associated minimum dimensionless density which characterizes the maximum pollutant concentration at different locations. Due to the symmetry with respect to the plume center line, only half of the cross-section is shown. In this case, the ground effect is negligible since $H_T = 30$. It is clear that, as indicated before, the center of the plume is higher than the centroid (mass mean height). The figure shows that a plume experiences three stages after its release:

(1) A very short acceleration stage, during which the deformation of the plume is very small, i.e. the plume rises like a solid body. The rising vertical velocity of the plume increases at an almost constant acceleration.

(2) A long double-vortex stage, during which vorticity generated on both sides of the plume forms two large-scale eddies tightly wound around the two horizontal ends of the plume. During this rollup stage, large entrainment of outside air into the plume core takes place on the lower side.

(3) A plume breakup stage, during which the plume is divided into two major lumps and several small blobs which diffuse much like passive pollutant. This stage can be also called bifurcation stage. Clearly, the plume dispersion in this way is more efficient than the uniform plume dispersion as described by Gaussian models.

The mechanism of vorticity generation due to buoyancy, which is responsible for the evolution observed here, can be understood by examining the vorticity equation, equation (10). The vorticity generation term is proportional to the horizontal density gradient when, for simplicity, the Boussinesq approximation is invoked. For a plume of initially elliptical shape, the two large-scale, counter-rotating, streamwise vortices are formed due to the opposite horizontal density gradient, as shown in Fig. 8a, leading to a large-scale rollup which changes the plume shape significantly from that described by the traditional Gaussian type concentration distribution. The two eddies induce a velocity field which moves the plume upwards. After this large-scale rollup, the plume–air interface is stretched and distorted, secondary vortices, with the same or the opposite sign of vorticity,

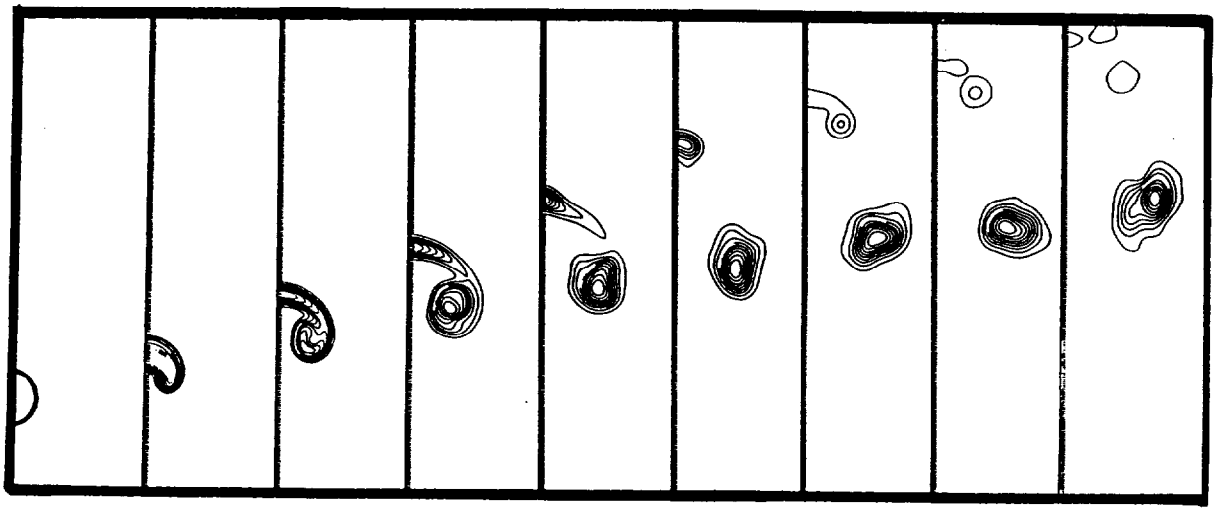

x	0	2	4	6	8	10	12	14	16
$\rho_{p,min}$	-1.00	-1.00	-0.81	-0.74	-0.70	-0.64	-0.63	-0.57	-0.50

Fig. 7. The evolution of the cross-section of a plume with $A_R = 1$, $H_T = 30$, and $Re_b = 10^3$ shown at different downwind locations, x. The corresponding minimum dimensionless deficient plume density are listed in the table. All frames are from $z = 28$ to 38 and the horizontal scale is the same as z.

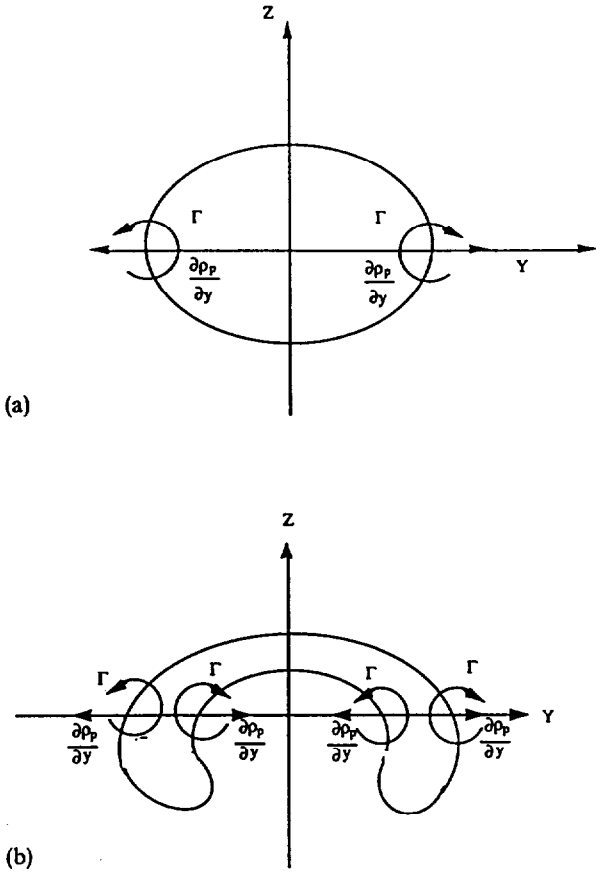

Fig. 8. A schematic diagram showing the mechanism of (a) large-eddy generation and (b) small-eddy generation.

are generated and the plume motion becomes turbulent as shown in Fig. 8b. In all stages, turbulence within the plume is far from Gaussian, and the plume dynamics resemble that of a trailing vortex behind an aircraft rather than that of a homogeneous turbulence field.

While the plume trajectory appears to be insensitive to the Reynolds number, or small scale diffusion, the entrainment and mixing within the plume cross-section are related. Figure 9 shows the plume cross-sections at $x=4.5$ for four different buoyancy Reynolds numbers. In all cases, the formation of the two large vortices on the sides of the plume contributes significantly to the redistribution of the plume material. The density field is smoother at lower Reynolds number. Figure 10 depicts the development of the plume cross-section at high Reynolds number, $Re_b=10^5$. The patterns of the large-eddy formation and small eddy generation are shown. The small-scale perturbations developed at the top surface are rapidly growing along the vortex sheet, rolling into small eddies and propagating down towards the bottom side.

A detailed description of the acceleration stage, which is important in calculating the circulation of the two large eddies that govern the plume buoyant dynamics, has not been given in the literature (Turner, 1959). In this work, this total circulation is evaluated from the numerical results and is displayed in Fig. 11. The total circulation is obtained by summing over the circulation of all the vortex elements which lie on either side of the symmetry line, i.e. for one-half of the plume cross-section. As shown in the figure, right after the acceleration stage, the total circulation reaches a constant value and is sustained for a long time (at least up to the termination of our calculation, $x=17.5$), consistent with Turner's hypothesis. This is somewhat surprising since the plume cross-section continues to deform. To reconcile these two observations, we examine the two components of vorticity whose summation lead to the total circulation (see Fig. 8b). Figure 11 shows the positive circulation, obtained by summing over the elements whose circulation is positive; the negative circulation, obtained by summing over the elements whose circulation is negative. The total circulation can also be obtained by algebraically adding the positive and negative circulations. As expected from the schematic diagrams in Fig. 8, while the negative circulation grows steadily, secondary rollup forms positive circulation which, at the late stages, grows at the same rate as that of the negative circulation. Thus, beyond the early large-scale rollup stage, the total circulation on either side of the plume remains constant.

As mentioned before, Turner (1959) suggested a model in which the plume dynamics are represented by a pair of streamwise vortices of a given circulation which remains constant during the plume dispersion phase. Our results suggest that this model, although crude, may be a reasonable representation of some aspects of plume motion and that the total circulation of the large structure indeed converges towards a constant value. It is apparent that the saturation of the total circulation and the fact that the kidney-shaped coherent structure is fairly long-lived is what makes the entrainement assumption in integral models approximately valid. It is interesting to note that in the normalized variables used here, the total circulation is of order unity.

Since the dynamics of the plume cross-section can be approximately modeled by two windwise line vortices, the weak effect of a flat ground terrain shown in Fig. 4 can be justified by considering the interaction between the vortices and their two images, as illustrated in Fig. 12. Since the induced velocity by a vortex decays away from its center as $1/|\tilde{x}-\tilde{x}_v|$, where $\tilde{x}_v$ is the vortex center, and since in this case $|\tilde{x}-\tilde{x}_v|$ is proportional to twice the initial plume height, the ground effect weakens as H_T increases from 1 to 30. As shown in Fig. 12, the net velocity induced by the images on the plume has a horizontal component pointing towards the plume center. Thus, when the ground effect is measurable, it leads to a reduction in the horizontal spread. Let W, the maximum horizontal distance between any two computational elements, represent the width of the plume in the y-direction. Figure 13 shows $W(x)$ of two plumes, with and without the ground effect. In both cases, the width of the

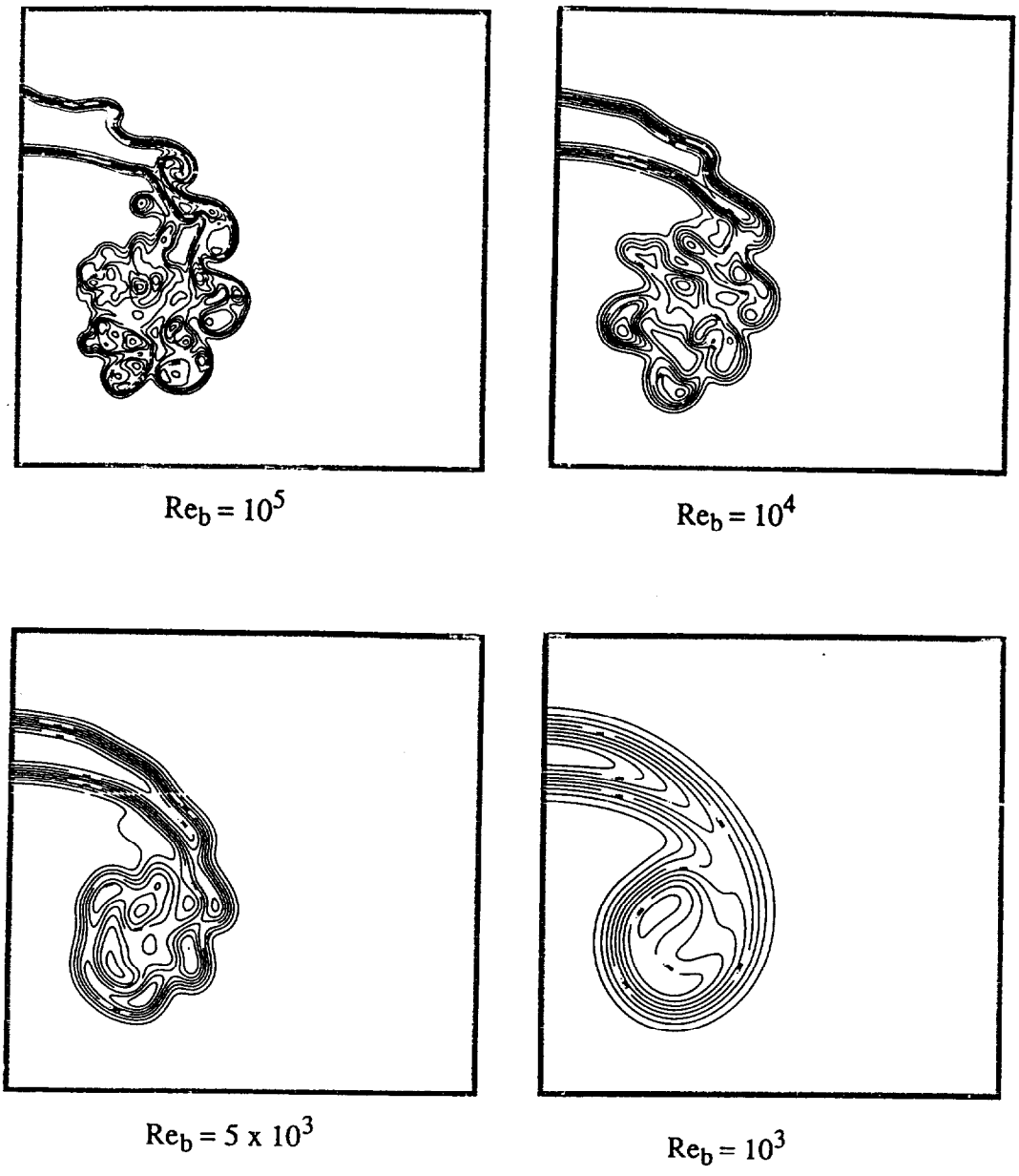

Fig. 9. Plume cross-sections shown for different buoyant Reynolds numbers for $A_R = 1$, $H_T = 30$, at $x = 4.5$. All frames are from $y = 0$ to 2.5 and $z = 30.5$ to 33.5.

plume grows almost linearly with the downwind distance x. The presence of kinks is mainly due to the non-uniform rollup of the eddies. Without the ground effect, the plume expands slightly faster. Within the limitations of this model, the results suggest that the ground effect on the plume width is negligible. This is similar to the conclusion reached before regarding the ground effect on the plume trajectory. As mentioned before, wind shear effect may change these conclusions, especially close to the ground.

The effect of the aspect ratio of the plume cross-section on the plume trajectory, shown in Fig. 5, can be explained by the rate of vorticity generation along the plume surface and its dependence on the plume shape. Since the rate of vorticity generation is proportional to $\partial \rho_p / \partial y$, for plumes of same cross-sectional area, a large A_R-plume has smaller portion of interface where vorticity can be generated. Thus, in the early stages, the rise of a large A_R-plume is slower than that of a small A_R-plume. However, the faster generation of vorticity also accelerates the entrainment process, thus limits the buoyancy strength hence eventually delaying its rise after $x = 15$.

5.3. *Entrainment and entrainment assumptions*

There has been a growing realization that the transport properties of many turbulent shear flows are dominated by semi-deterministic large-scale vortex structures. Turner (1986) proposed using large-scale engulfment as a basis for the entrainment hypothesis. Viscous diffusion may only be important at the final digestion of external fluid into the turbulent flow and the evolution of the smaller-scale motions, but not in determining the overall rate of mixing.

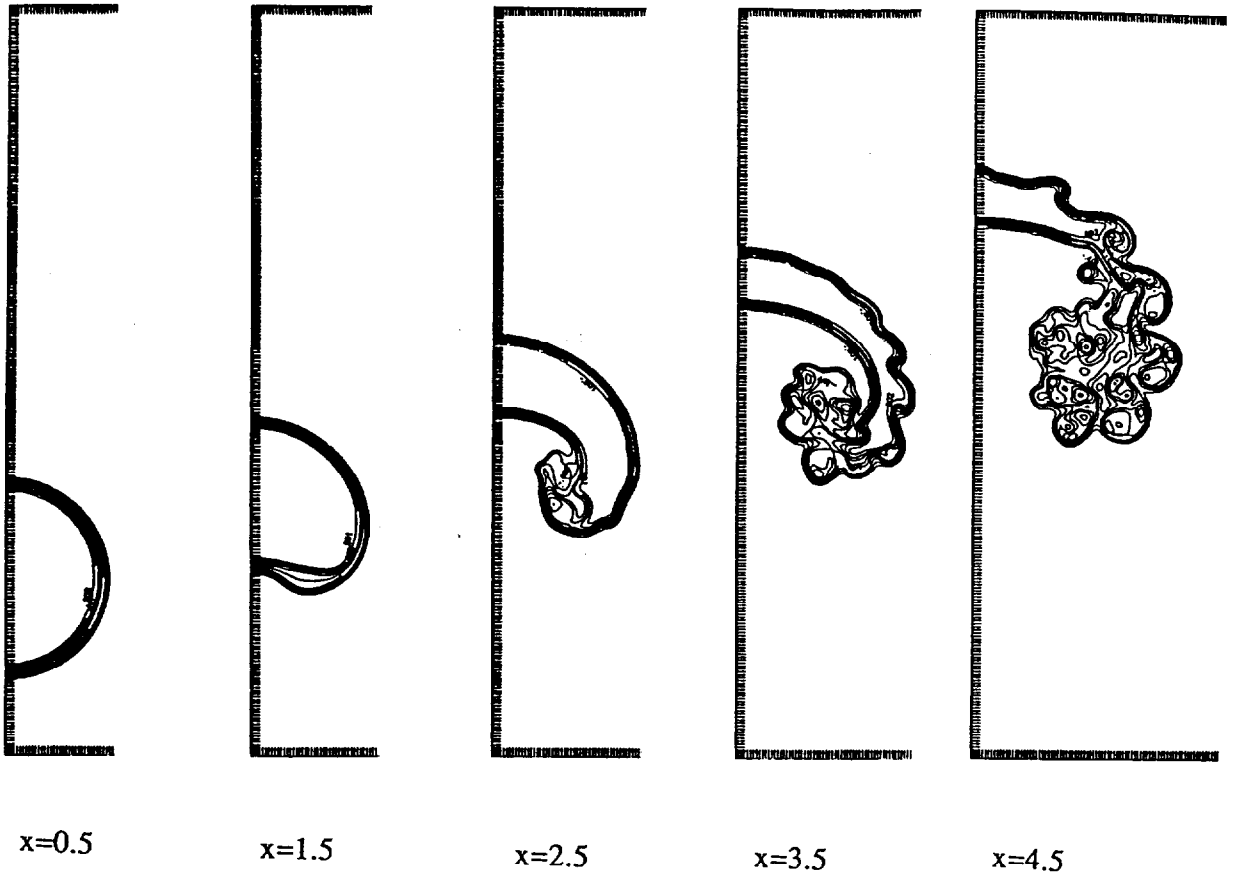

Fig. 10. The evolution of the cross-section of a plume at different downwind locations for $A_R=1$, $H_T=30$, and $Re_b=10^5$. All frames are from $z=29.0$ to 33.5 and $y=0.0$ to 4.5.

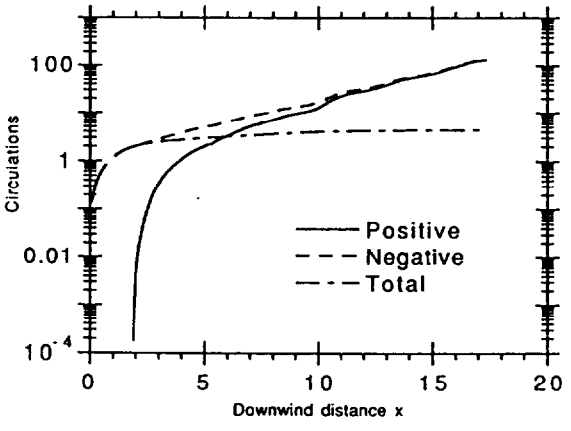

Fig. 11. Absolute values of the positive circulation, negative circulation, and the sum of the two (total circulation), taken over the right half of the plume, $A_R=1$, $H_T=30$, and $Re_b=10^3$.

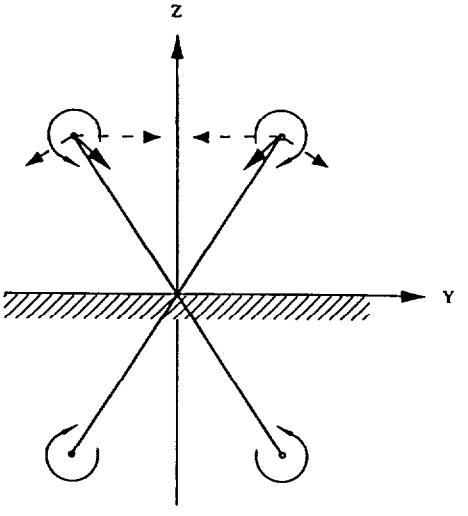

Fig. 12. Schematic diagram showing the ground effect on the plume rise and dispersion. Dashed arrows are the velocity vectors induced by two images. The solid arrows acting on the vortices are the image-induced total velocity vectors.

Our numerical simulation confirms these observations. Figure 14a shows the induced velocity in the plume cross-section. For comparison, the unit velocity vector and the plume surface are also shown on the same plot. The material surrounding the plume is engulfed toward its center from below. Most of the entrainment into the plume core is induced by the two large eddies. The entrainment is thus neither homogeneous nor isotropic. Clearly, the nearby atmosphere is disturbed due to the presence of the plume, and the density distribution within the plume is distorted due to this large-scale entrainment. The strong wind and swirling motion often observed in the presence of a fire can be explained by the powerful entrainment

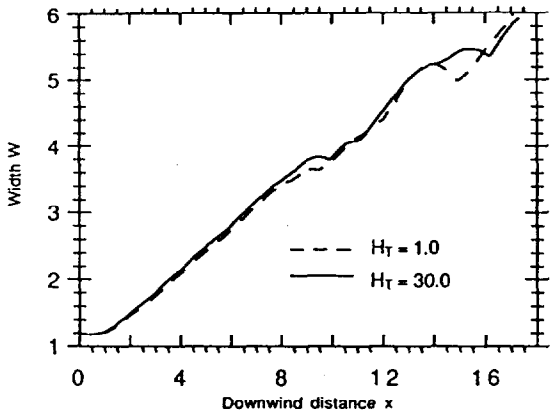

Fig. 13. The plume width vs downwind distance x with and without ground effect. Both cases have $A_R = 1$ and $Re_b = 10^3$.

currents established by the dynamic field of a rising plume as represented by the two large eddies. Figure 14b shows the plume motion in terms of the locations and velocity vectors of the computational elements used to discretize the outer surface of the plume cross-section.

The total inflow at any position x depends on the geometry and dynamics of the flow. From experimental measurements, the entrainment constant in equation (A7) is often taken as $\beta = 0.4$, which is different from $\beta = 0.6$ used in equation (23). This inconsistency in the integral model has been pointed out by numerous authors (Briggs, 1975). Since the plume is not of exact circular form, we define an equivalent radius R_{eq} so that

$$\pi R_{eq}^2 = \frac{\pi}{4} H \cdot W \tag{25}$$

where H is the maximum vertical extension of the plume cross-section, defined here as the distance between the highest and lowest computational elements, representing the plume vertical thickness. From our numerical solution, following the acceleration stage, R_{eq} is found to change almost linearly with x, almost independent of to the aspect ratio and the plume release height, as shown in Figs 15a and b.

5.4. *Plume circumference*

Another measure of entrainment is the circumference of the plume cross-section, defined by the summation of the distances between adjacent computational elements along the interface between the plume material and air. Since the plume surface is wrinkled due to local vorticity generation, the actual periphery is much longer than that calculated by simple circular or elliptical circumferences. During the acceleration stage, there is not much variation of this length as the plume rises undistorted, as shown in Fig. 16 for $x \leqslant 1.5$. The stretching of the circumference is distinctly faster during the small-scale rollup, when several areas of plume experience local stretching around concentrated vortices, than during the large-scale rollup. While the ground effect is negligible, the circumference increases faster for smaller A_R which is consistent with the fact that this plume experiences stronger vorticity generation.

Comparison between Figs 15 and 16 shows that the equivalent radius is a better measure of entrainment since the length of the plume suffers from the evolution of several small eddies which do not contribute significantly to entrainment. We also note that the size and strength of the small scales is a function of the buoyancy Reynolds number, as shown in Fig. 9.

6. THE BOUSSINESQ APPROXIMATION

In practice, the Boussinesq approximation is a convenient simplification when small density variations

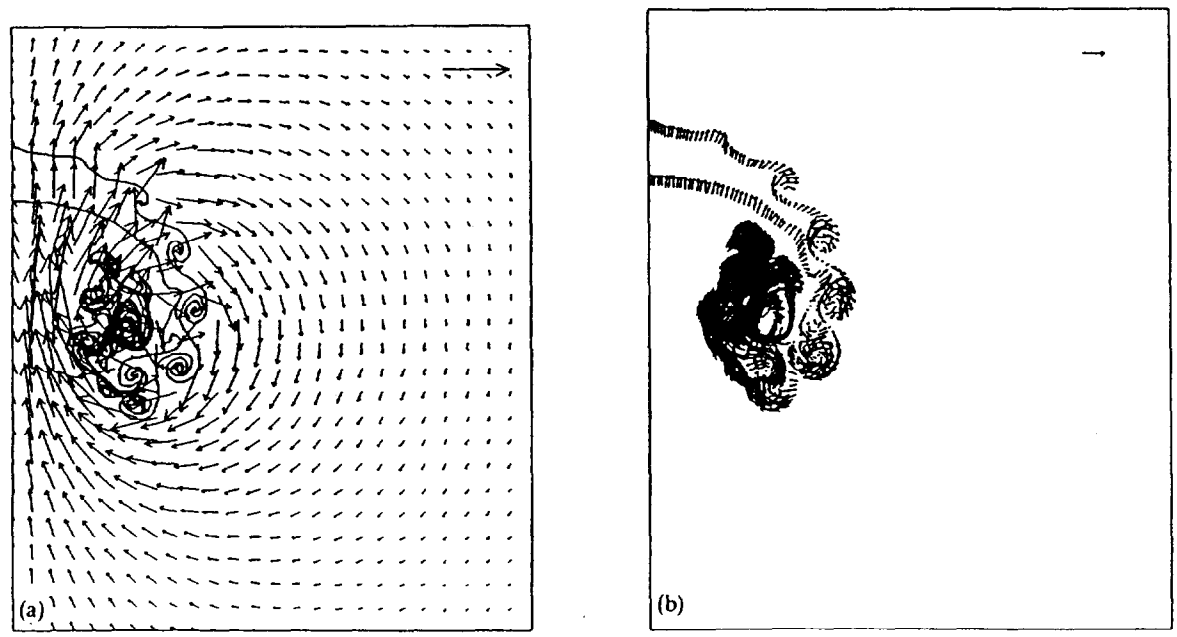

Fig. 14. (a) The buoyancy-induced velocity field and plume outer surface for $Re_b = 10^5$, $A_R = 1$, and $H_T = 30$ at $x = 4$, and (b) positions and velocities of the computational elements. Both frames are from $z = 29.0$ to 33.0 and $y = 0.0$ to 3.0.

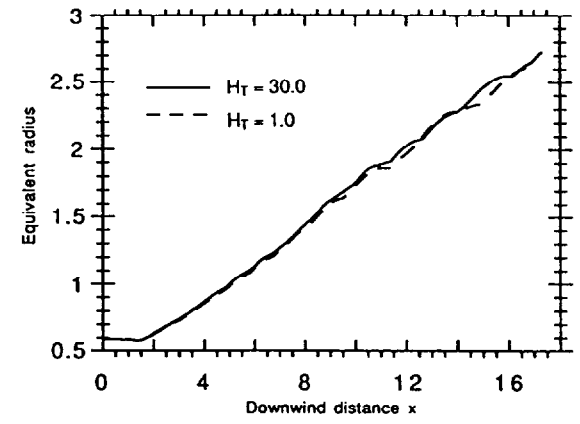

Fig. 15. Equivalent radius of the plume cross-section vs the downwind distance x, for $A_R = 1$, $Re_b = 10^3$ (a) with and without ground effect, (b) for different aspect ratios.

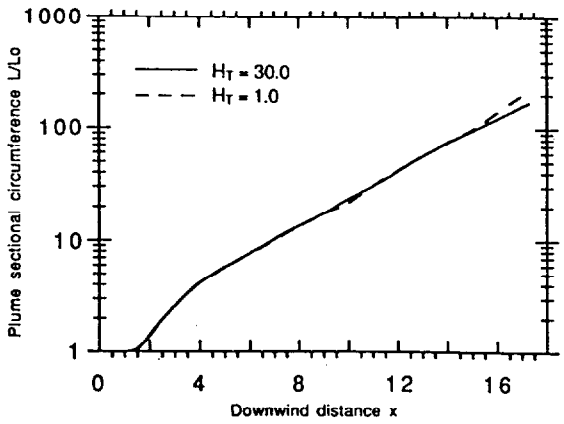

Fig. 16. Circumference of the plume cross-section vs downwind distance x, $A_R = 1$, $Re_b = 10^3$ (a) with and without ground effect, (b) with different aspect ratios.

are involved in fluid motion (Spiegel and Veronis, 1960). In many flows, including that of a plume, using the Boussinesq approximation renders the problem self-similar with respect to the density ratio and hence reduces the number of independent parameters. However, before using this approximation in extensive modeling, it is important to determine the limits within which the error introduced by the assumption is acceptable.

Invoking the Boussinesq approximation is equivalent to setting $\varepsilon = 0$ in the vorticity and momentum equations. We performed numerical experiments at $\varepsilon = |\rho_p^*/\rho_o^*| = 0$, 0.01, 0.1 and 0.5 for an initially circular plume at $H_T = 30$ with $Re_b = 10^3$, to study the effect of the Boussinesq approximation on the solution for different density ratios.

Figures 17 and 18 show the plume trajectory and equivalent radius, respectively. The curves corresponding to cases with $\varepsilon = 0$, 0.01 and 0.1 are almost indistinguishable. This suggests that the Boussinesq approximation is valid when $\varepsilon \leqslant 0.1$, i.e. when, in the case of a plume with a circular cross-section, the density ratio $|\rho_p^*/\rho_o^*| \leqslant 0.1$. This restriction may be relaxed somewhat depending on the inaccuracies allowed in the calculation. For most fire and exhaust plumes, $\varepsilon \leqslant 0.1$ is usually satisfied.

The curve with $\varepsilon = 0.5$, i.e. $|\rho_p^*/\rho_o^*| = 0.5$, shows some departure, which increases at a longer time, from the Boussinesq approximation solution. It is evident that the Boussinesq approximation underestimates the plume rise and equivalent radius.

7. CONCLUSION

A Lagrangian model of buoyant plume rise and dispersion in a calm neutral atmosphere is developed in connection with vortex and transport element methods. The computed plume trajectory is compared with the experimentally based two-thirds power law. The transition from the early stages of buoyancy-dominated plume to the later stages, when atmospheric turbulence begins to dominate the plume motion, is calculated. The main conclusions of this study are summarized in the following.

(1) The plume trajectory is insensitive to the small-scale atmospheric turbulence. The plume trajectory,

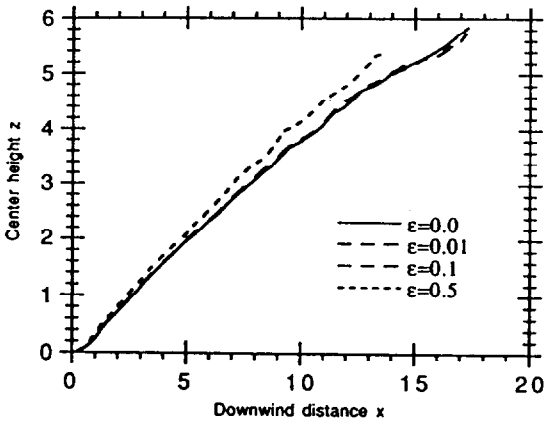

Fig. 17. Center plume trajectory for $A_R=1$, $H_T=30$, and $Re_b=10^3$, with different deficient mass flux ratios.

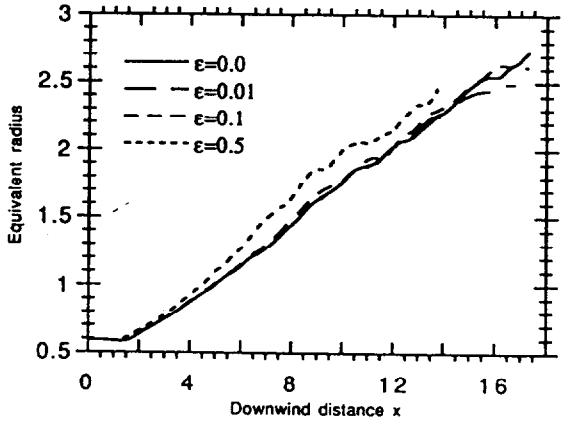

Fig. 18. Equivalent radius of the plume cross-section, for $A_R=1$, $H_T=30$, $Re_b=10^3$, with different deficient mass flux ratios.

for the case of $A_R=1$, follows closely the extended two-thirds power law.

(2) The plume experiences three stages which have distinctive characteristics; (i) a short acceleration stage, (ii) a long double-vortex stage, and (iii) a plume breakup stage.

(3) The plume cross-section is found to be kidney-shaped. The process of double-vortex formation and plume bifurcation can be explained by the baroclinic vorticity generation mechanism.

(4) The effect of a flat ground on the plume trajectory and dispersion is small.

(5) The aspect ratio of the plume cross-section is an important parameter. Large A_R plume rises slower initially and then catches up with small A_R plumes during the breakup stage.

(6) The entrainment field is dominated by large-scale engulfment which is neither isotropic nor homogeneous.

(7) The Boussinesq approximation is valid for $\varepsilon=|\rho_p^*/\rho_o^*|\leqslant 0.1$.

The long-term plan of our effort is to extend the modeling approach introduced in this paper to include several important effects such as: (a) atmospheric density stratification; (b) wind shear; and (c) atmospheric turbulence of scales comparable to and larger than the plume characteristic dimension. The parabolization of the equations in the wind direction introduced here, which, in essence, restricts the vorticity to the streamwise component only and treats the flow within the plume cross-section as being two-dimensional, is expected to be sufficient in the study of (a). However, in order to investigate (b) and (c), the other vorticity components will have to be included in the formulation and the three-dimensional problem be treated in full.

Acknowledgement—This work has been jointly supported by the Mineral Management Services of the Department of the Interior and the Building and Fire Research Laboratory of the National Institute of Standard and Technology. We wish to acknowledge Dr Howard Baum of NIST for his contribution to the formulation and many helpful discussions. The computer support for this project has been provided by the Illinois National Center for Supercomputer Applications.

REFERENCES

Abdelwahed M. A. T. and Chu V. H. (1978) Bifurcation of buoyant jets in cross flow. Technical Report 78-1, Dept. Civ. Eng., McGill Univ., 130pp.

Beale J. T. and Majda A. (1982a) Vortex method 1: convergence in three dimensions. *Math. Comput.* **39**, 1–27.

Beale J. T. and Majda A. (1982b) Vortex method 2: higher order accuracy in two and three dimensions. *Math. Comput.* **39**, 28–52.

Briggs G. A. (1975) Plume rise predictions. *Lectures on Air Pollution and Environmental Impact Analysis* (edited by Haugen D. A.), pp. 59–11. American Meteorological Society, Boston, U.S.A.

Briggs G. A. (1984) Plume rise and buoyancy effects. In *Atmospheric Science and Power Production* (edited by Randerson D.), pp. 327–366. U.S. Dept. of Energy DOE/TIC-27601, available from NTIS as DE84005177.

Crabb D., Durao D. F. G. and Whitelaw J. H. (1981) A round jet normal to a crossflow. *Trans. ASME* **103**, 142–153.

Csanady G. T. (1965) The buoyant motion within a hot gas plume in a horizontal wind. *J. Fluid Mech.* **22**, 225–239.

Csanady G. T. (1973) *Turbulent Diffusion in the Environment.* D. Reidel, Dordrecht.

Dahlquist G. and Björck A. (1974) *Numerical Methods.* Prentice Hall, New York.

Deardorff J. W. (1970) Convective velocity and temperature scales for the unstable planetary boundary layer. *J. atmos. Sci.* **27**, 1211–1213.

Evans D., Baum H., McCaffrey B., Mulholland G., Harkleroad M. and Manders W. (1986) Combustion of Oil on Water. Report NBSIR 86-3420, National Bureau of Standards, Gaithersburg, MD 20899.

Evans D., Baum H., Mulholland G., Bryner N. and Forney G. (1989) Smoke Plumes From Crude Oil Burns. NISTIR Report, National Institute of Standard and Technology.

Fanaki F. H. (1975) Experimental observations of a bifurcation buoyant plume. *Boundary-Layer Met.* **9**, 479–495.

Fay J. A., Escudier M. and Hoult D. P. (1970) A correlation of field observations of plume rise. *J. Air Pollut. Control Ass.* **20**, 391–397.

Gebhart B., Hilder D. S. and Kelleher M. (1984) The diffusion of turbulent buoyant jets. *Int. J. Heat Mass Transfer* **27**, 1–57.

Ghoniem A. F., Heidarinejad G. and Krishnan A. (1988a) On

mixing, baroclinicity and the effect of strain in a chemically reacting shear layer. The AIAA 26th Aerospace Science Meeting, Reno, NV, 11–15 January, AIAA-88-0729 and the 22nd Symposium (International) on Combustion, Sydney, Australia, July 1992, The Combustion Institute, Pittsburgh, PA.

Ghoniem A. F., Heidarinejad G. and Krishnan A. (1988b) Numerical simulation of a thermally stratified shear layer using the vortex element method. *J. Comput. Phys.* **79**, 135–166.

Ghoniem A. F., Zhang X. and Knio O. M. (1991) First Annual Report on Development of a Computational Model for Smoke Plume Dispersion and Deposition, NIST, National Institute of Standard and Technology, Gaithersburg, MD 20899, U.S.A.

Ghoniem A. F., Zhang X., Knio O. M., Baum H. and Rehm R. (1992) Dispersion and deposition of smoke plumes generated from massive fires. *J. Hazard Mat.* **33**, 275–293.

Gifford F. A. (1975) Atmospheric dispersion models for environmental pollution applications. *Lecture on Air Pollution and Environmental Impact Analyses* (edited by Haugen D. A.), pp. 35–58. American Meteorological Society, Boston, U.S.A.

Golay M. W. (1982) Numerical modeling of buoyant plumes in a turbulent, stratified atmosphere. *Atmospheric Environment* **16**, 2373–2381.

Hewett T. A., Fay J. A. and Hoult D. P. (1971) Laboratory experiments of smokestack plumes in a stable atmosphere. *Atmospheric Environment* **5**, 767–789.

Janseen L. H. J. M., Nieuwstadt F. T. M. and Donze M. (1990) Time scales of physical and chemical processes in chemically reactive plumes. *Atmospheric Environment* **24A**, 2861–2874.

Khandekar M. L. and Murty T. S. (1975) A note on bifurcation of buoyant bent-over chimney plumes. *Atmospheric Environment* **9**, 759–762.

Knio O. M. and Ghoniem A. F. (1991) Three-dimensional vortex simulation of rollup and entrainment in a shear layer. *J. Comput. Phys.* **97**, 172–223.

Knio O. M. and Ghoniem A. F. (1992) The three-dimensional structure of periodic vorticity layers under nonsymmetric conditions. *J. Fluid Mech.* **243**, 353–392.

Krishnan A. and Ghoniem A. F. (1992) Simulation of rollup and mixing in Rayleigh–Taylor flow using the transport element method. *J. Comput. Phys.* **99**, 1–27.

Lilly D. K. (1964) Numerical solution for the shape-preserving two-dimensional thermal convection element. *J. atmos. Sci.* **21**, 83–98.

Luti F. M. and Brzustowski T. A. (1977) Flow due to a two-dimensional heat source with cross flow in the atmosphere. *Comb. Sci. Tech.* **16**, 71–87.

McMahon H. M., Hester D. D. and Palfery J. G. (1971) Vortex shedding from a turbulent jet in a cross wind. *J. Fluid Mech.* **48**, 73–80.

Meng J. C. S. and Thomson J. A. L. (1978) Numerical studies of some nonlinear hydrodynamic problems by discrete vortex element methods. *J. Fluid Mech.* **84**, 433–453.

Moore D. J. (1966) Physical aspects of puff models. *Int. J. Air Water Pollut.* **10**, 411–417.

Netterville D. D. J. (1990) Plume rise, entrainment and dispersion in turbulent wind. *Atmospheric Environment* **24A**, 1061–1081.

Nieuwstadt F. T. M. (1992a) A large-eddy simulation of a line source in a convective atmospheric boundary layer—1. Dispersion characteristics. *Atmospheric Environment* **26A**, 485–495.

Nieuwstadt F. T. M. (1992b) A large-eddy simulation of a line source in a convective atmospheric boundary layer—2. Dynamics of a buoyant line source. *Atmospheric Environment* **26A**, 497–503.

Schwartz J. and Tulin M. P. (1972) Chimney plumes in neutral and stable surroundings. *Atmosphric Environment* **6**, 19–35.

Scorer R. S. (1958) *Natural Aerodynamics*, pp. 143–217. Pergamon Press, New York.

Seinfeld J. H. (1986) *Atmospheric Chemistry and Physics of Air Pollution*. John Wiley, New York.

Sherif S. A. and Pletcher R. H. (1989) Measurements of the flow and turbulence characteristics of round jets in crossflow. *J. Fluid Engng* **111**, 165.

Spiegel E. A. and Veronis G. (1960) On the Boussinesq approximation for a compressible fluid. *J. Astrophys.* **131**, 442–447.

Sykes R. I. (1988) Concentration fluctuations in dispersing plumes. In *Lectures on Air Pollution Modeling* (edited by Venkatram A. and Wyngaad J. C.), pp. 325–356. American Meteorological Society, Boston, U.S.A.

Tsang G. (1971) Laboratory study of line thermals. *Atmospheric Environment* **5**, 445–471.

Turner D. B. (1970) *Workbook of Atmospheric Dispersion Estimates*, U.S. Environmental Protection Agency, Office of Air Programs, Ref. No. AP-26, 84pp.

Turner J. S. (1959) A comparison between buoyant vortex rings and vortex pairs. *J. Fluid Mech.* **7**, 419.

Turner J. S. (1986) Turbulent entrainment: the development of the entrainment assumption, and its application to geophysical flows. *J. Fluid Mech.* **173**, 431–471.

Venkatram A. (1988) Dispersion in the stable boundary layer. In *Lectures on Air Pollution Modeling* (edited by Venkatram A. and Wyngaard J. C.), pp. 229–265 American Meteorological Society, Boston, U.S.A.

Weil J. C. (1988a) Plume rise. In *Lectures on Air Pollution Modeling* (edited by Venkatram A. and Wyngaard J. C.), pp. 119–166. American Meteorological Society, Boston, U.S.A.

Weil J. C. (1988b) Dispersion in the convective boundary layer. In *Lectures on Air Pollution Modeling* (edited by Venkatram A. and Wyngaard J. C.), pp. 167–227. American Meteorological Society, Boston, U.S.A.

Zhang X. and Ghoniem A. F. (1993) A computational model for the rise and dispersion of wind-blown, buoyancy-driven plumes—II. Linearly stratified atmosphere. *Atmospheric Environment* (submitted).

APPENDIX

The motion of a buoyant plume can be modeled by the following equations (Briggs, 1984)

$$U\frac{dR^{*2}}{dx^*}=2\beta w^* R^* \tag{A1}$$

$$U\frac{d(R^{*2}w^*)}{dx^*}=R^{*2}g_r\frac{\Delta\rho^*}{\rho_o^*} \tag{A2}$$

$$U\frac{d}{dx^*}\left(R^{*2}g_r\frac{\Delta\rho^*}{\rho_o^*}\right)=0 \tag{A3}$$

pertaining, respectively, to the conservation of mass (entrainment assumption), momentum and energy, where R^* is the radius of the plume cross-section, w^* is the vertical velocity of the plume, ρ_o^* is a reference density, taken as the ambient air density, $\Delta\rho^*$ is the density difference between the plume and surrounding at downwind location x^*, U is the mean wind speed, g_r is the gravitational acceleration and β is an entrainment constant. In the above equations it is assumed that U is uniform and that the plume density and vertical velocity have "top-hat" profiles (i.e. constant $\Delta\rho^*$ and w^* from 0 to R^*). Moreover

$$w^*=U\frac{dz^*}{dx^*} \tag{A4}$$

$$R^*(x^*=0)=R_o^* \tag{A5}$$

$$z^*(x^*=0)=0 \tag{A6}$$

where z^* is the mean plume rise, R_o^* is the radius of the initial plume size. Equations (A1) and (A4) show that

$$R^* = R_o^* + \beta z^*. \tag{A7}$$

In a neutrally stratified atmosphere, equation (A3) shows that

$$R^{*2} g_r \frac{\Delta\rho^*}{\rho_o^*} = \text{constant} = \frac{F_b}{U} \tag{A8}$$

where $F_b = |\rho_p^*/\rho_o^*|\ R_o^{*2} U g_r$ is the buoyancy flux. From equations (A2) and (A4), we find that

$$R^{*2} \frac{dz^*}{dx^*} = \frac{F_b}{U^3} x^*. \tag{A9}$$

Combining equations (A5), (A7) and (A9), we obtain the following expression for the plume height

$$(\beta z^* + R_o^*)^3 - R_o^{*3} = \frac{3\beta F_b}{2U^3} x^{*2}. \tag{A10}$$

This is the extended two-thirds law. If $\beta z^* \gg R_o^*$, the conventional two-thirds law for a point source plume is recovered. Using the procedure outlined in Section 2, we can write equation (A10) in dimensionless form: the x-direction length scale is $l_x = U\sqrt{(R)/(|\rho_p^*/\rho_o^*|\, g_r)}$ and the length scale in both y and z directions is $l_y = R$. The buoyancy length scale in equation (22) can be written in terms of the scales used in this study as

$$\pi l_b = \frac{l_y^3}{l_x^2}. \tag{A11}$$